

1
2
3
4
5
6
7
8
9
10
11
12
13
14
15
16
17
18
19
20
21
22
23
24
25
26
27
28
29
30
31
32
33
34
35
36
37
38
39
40
41

Robust latent-variable interpretation of *in vivo* regression models by nested resampling

Alexander W. Caulk¹ & Kevin A. Janes^{2,3,*}

¹Department of Biomedical Engineering, Yale University, New Haven, CT, 06510, USA

²Department of Biomedical Engineering, University of Virginia, Charlottesville, VA, 22908, USA

³Department of Biochemistry & Molecular Genetics, University of Virginia, Charlottesville, VA, 22908, USA

Keywords: systems biology, partial least squares regression, vascular mechanics, inflammation, angiotensin II, tumor necrosis factor α

Word and item count:

Text = 5038

Abstract = 200; References = 58; Figures = 9; Tables = 3

*Correspondence and requests for materials should be addressed to K.A.J. (kjanes@virginia.edu)

42 **ABSTRACT**

43 Simple multilinear methods, such as partial least squares regression (PLSR), are effective
44 at interrelating dynamic, multivariate datasets of cell–molecular biology through high-dimensional
45 arrays. However, data collected *in vivo* are more difficult, because animal-to-animal variability is
46 often high, and each time-point measured is usually a terminal endpoint for that animal.
47 Observations are further complicated by the nesting of cells within tissues or tissue sections, which
48 themselves are nested within animals. Here, we introduce principled resampling strategies that
49 preserve the tissue-animal hierarchy of individual replicates and compute the uncertainty of
50 multidimensional decompositions applied to global averages. Using molecular–phenotypic data
51 from the mouse aorta and colon, we find that interpretation of decomposed latent variables (LVs)
52 changes when PLSR models are resampled. Lagging LVs, which statistically improve global-
53 average models, are unstable in resampled iterations that preserve nesting relationships, arguing
54 that these LVs should not be mined for biological insight. Interestingly, resampling is less
55 discriminatory for multidimensional regressions of *in vitro* data, suggesting it is unnecessary when
56 replicate-to-replicate variance is low. Our work illustrates the challenges and opportunities in
57 translating systems-biology approaches from cultured cells to living organisms. Nested resampling
58 adds a straightforward quality-control step aiding the interpretability of *in vivo* regression models.
59

60 INTRODUCTION

61 Modern biology and physiology demand rich, quantitative, time-resolved observations
62 obtained by different methods¹. To analyze such datasets, statistical “data-driven” modeling²
63 approaches have been productively deployed *in vitro* to examine network-level relationships
64 between signal transduction and cell phenotype³⁻⁹. One class of models uses partial least squares
65 regression (PLSR) to factorize data by the measured biological variables¹⁰. Linear combinations
66 are iteratively extracted as latent variables (LVs) that optimize the covariation between
67 independent and dependent datasets to enable input-output predictions. Highly multivariate data
68 are efficiently modeled by a small number of LVs because of the mass-action kinetic processes
69 underlying biological regulation¹¹.

70 The success of PLSR at capturing biological function extends to nonlinear derivatives¹²
71 and structured multidimensional data arrays¹³ (tensors) from cell lines. By contrast, *in vivo*
72 applications of PLSR have not gone beyond qualitative classification of inputs or outcomes¹⁴⁻¹⁷.
73 The gap is unfortunate, because *in vivo* studies are the gold standard to compare phenotypes across
74 species^{18,19}, disease models^{20,21}, and laboratories²²⁻²⁶. Animal surrogates can offer insight into the
75 (patho)physiologic function of individual proteins, but interpreting the consequences of *in vivo*
76 perturbations is complicated^{27,28}. Applying PLSR quantitatively to *in vivo* data may better identify
77 the underlying networks that, when perturbed, yield clinically relevant phenotypes.

78 For predictive modeling, there are many hurdles to using PLSR- and other LV-based
79 approaches with *in vivo* data. Unlike spectroscopy (where PLSR originated¹⁰) or experiments in
80 cultured cells, variation among *in vivo* replicates is often large even within inbred strains²⁹⁻³¹, and
81 this uncertainty does not get transmitted to standard models built from global averages. Including
82 all replicates fixes the problem but creates others related to crossvalidation³² and the nesting of

83 replicates in the study design³³. *In vivo* data are typically grouped by replicate within a time point
84 but are unpaired between time points, complicating model construction. An open question is
85 whether the combinatorics of replicated, multivariate *in vivo* datasets can be tackled
86 algorithmically within a multidimensional PLSR framework.

87 In this study, we apply computational statistics³⁴ to the construction and interpretation of
88 *in vivo* PLSR models built from multidimensional arrays (Fig. 1). Replicate-to-replicate
89 uncertainty is propagated by resampling strategies that maintain the nesting relationships of the
90 data acquisition. Nested resampling separates robust latent variables, which arise regardless of
91 replicate configuration, from those that are statistically important in the global-average model but
92 fragile upon resampling. Interpretations of robustness are more conservative when nested
93 resampling is executed by bootstrapping (a leave-one-in approach) than by jackknifing (a leave-
94 one-out approach). By contrast, neither is especially informative at discriminating latent variables
95 when applied to a highly reproducible³⁵ multidimensional dataset collected *in vitro*, bolstering the
96 claims of earlier studies with cultured cells³⁻⁹. By leveraging the structure of multidimensional
97 arrays, nested resampling provides a rapid numerical means to incorporate the uncertainty of *in*
98 *vivo* observations into data-driven models without violating their mathematical assumptions.

99

100 **RESULTS**

101 We sought an implementation of PLSR that robustly analyzes *in vivo* datasets comprised
102 of temporal, multiparameter, and interrelated responses to perturbations. At the core of a PLSR
103 model are its LVs (alternatively, principal components), which capture separable covariations
104 among measured observations^{2,36}. Interpreting LV features—for example, a “score” related to a
105 condition or a “weight” (“loading”) related to a measured observation—is aided by computational

106 randomization approaches that build hundreds of null models from the same data but without any
107 true structure^{13,37}. Scores and loadings that are similar between the null model and the actual model
108 indicate data artifacts (biases, batch effects, etc.) that should not be used for hypothesis generation.
109 Thus, by systematically building many alternative models, the randomization approach
110 contextualizes the meaning of the true model.

111 We reasoned that a conceptually analogous approach might be useful for handling *in vivo*
112 datasets that are inherently more variable than is typical for PLSR^{31,32}. Iterative leave-one-out
113 approaches such as jackknifing³⁸ or crossvalidation¹⁰ are established approaches for omitting
114 individual conditions during PLSR training and validation. Unexplored is whether there could be
115 value in adapting such a strategy to replicates rather than conditions. To resample replicates by
116 jackknifing, one biological replicate (*i.e.*, animal) is randomly omitted from each condition. All
117 observations from that replicate are removed as a group to reflect the nesting relationships within
118 the dataset. After one replicate is left out, averages are recalculated and a resampled PLSR model
119 is built. The distribution of hundreds of jackknifed iterations indicates the extent to which the
120 global-average model requires all of the data available.

121 Reciprocally, one could ask whether the global-average model is sufficiently reconstructed
122 from any of the data by using bootstrapping instead of jackknifing. For bootstrap resampling, the
123 nested observations from one biological replicate (animal) are randomly selected from each
124 condition to build an n-of-one dataset that is modeled by PLSR. As with jackknife resampling,
125 hundreds of iterations are compiled, yielding a bootstrap distribution of models and LVs based on
126 a single instance of the data. Together, nested jackknife–bootstrap resampling should provide
127 numerical estimates for the fragility and robustness of PLSR models constructed from global-
128 average data with high inter-replicate variance.

129 The premise of nested resampling was tested in three contexts. First, we used a
130 multidimensional dataset from Bersi *et al.*³⁹ to build a new PLSR model, which warranted
131 reinterpretation after nested resampling. We next tested general applicability of the approach by
132 repurposing *in vivo* data from Lau *et al.*¹⁴ to construct a second multidimensional PLSR model for
133 nested-resampling analysis. Last, we asked whether the same tools were similarly informative
134 when applied to an existing multidimensional PLSR model from Chitforoushzadeh *et al.*¹³, which
135 was calibrated with highly reproducible data from cultured cells. The results collectively support
136 nested resampling as a useful complement to PLSR models applied to *in vivo* settings when
137 biological variability is large.

138

139 *Nested resampling uncovers PLSR model fragilities missed by randomization*

140 In the study by Bersi *et al.*³⁹, *ApoE*^{-/-} mice (used for their highly maladaptive hypertension-
141 induced vascular remodeling⁴⁰) were continuously administered Angiotensin II (AngII) and
142 evaluated for enzymatic, cellular, and mechanical changes in four regions of aortic tissue (Table
143 1). Enzymatic–cellular (immuno)histology was collected at three time points and mechanical data
144 at five time points over 28 days along with baseline controls ($N = 2–7$ animals; Fig. 2). For
145 multidimensional PLSR modeling, data were separated by histological (input) and mechanical
146 (output) data (Fig. 1) and standardized to predict mechanical metrics from histological and
147 immunohistochemical data (see Methods). The working hypothesis of the model was that
148 regionally disparate inflammatory and enzymatic changes in the aorta predictably drive differential
149 changes in tissue mechanical properties.

150 LVs were iteratively defined for the multidimensional arrays by established
151 approaches^{13,41}, and the model root mean squared error (RMSE) of prediction was minimized with

152 four LVs (Fig. 3a). By leave-one-out crossvalidation, we found that standardized predictions of
153 the four-LV model were accurate to within ~75% of the measured result when averaged across all
154 conditions (Fig. 3b), suggesting good predictive capacity. The four LVs of the multidimensional
155 PLSR model thereby parse the regional, temporal, and molecular–cellular–mechanical
156 covariations in the global-average dataset (Supplementary Fig. S1).

157 For LV interpretation and hypothesis generation from the Bersi *et al.*³⁹ dataset, we
158 compared existing randomization methods^{13,37} to nested resampling. Across the four LVs, nearly
159 all mechanical observations were weighted beyond the standard deviation of random null models
160 (Fig. 4a,b), supporting interpretation of the weights. For example, inner radius was positively
161 weighted on LV3 (ir; Fig. 4b) whereas thickness measures were negatively weighted on LV3 (H
162 and h; Fig. 4b), suggesting that LV3 may discriminate aneurysmal dilatation, which predisposes
163 to aortic dissection and rupture⁴², and fibrotic thickening, which predisposes to myocardial
164 infarction and stroke via increased arterial stiffness⁴³. However, interpretations changed when
165 biological variability of the underlying *in vivo* data was considered through nested resampling
166 (Fig. 4c–f). Both jackknifed and bootstrapped resampling suggested that LV3 and LV4 were too
167 unstable to justify interpreting any parameters in these LVs (Fig. 4d,f). LV1 and LV2 yielded
168 nonzero weights that were more robust, even retaining certain thickness and outer-diameter
169 observations that were excluded by randomization (H, od, and OD; Fig. 4c). However, nested
170 resampling revealed considerable uncertainty in the weights of LV3 and LV4 (Fig. 4d,f), arguing
171 against any quantitative comparison of mechanical observations along these LVs. In contrast to
172 standard performance metrics for PLSR (Fig. 3 and 4a,b), nested resampling provisioned the Bersi
173 *et al.*³⁹ model as fragile in its lagging LVs compared to the robustness of LV1 and LV2.

174 One possible explanation for such high uncertainty is that some resampled models might
175 switch the sign of an LV weight together with the associated LV score, which mutually offset as a
176 degenerate solution (Fig. 1). We accounted for sign switching by looking for symmetric bimodal
177 distributions about zero and flipping signs to the dominant mode when switching was evident.
178 Some bimodal scores were asymmetrically distributed with a near-zero mode (*e.g.*, the distribution
179 of LV1–LV2 scores for the DTA condition; Supplementary Fig. S2), indicating that their LV
180 assignments were heavily dependent on the resampling iteration. For LV3 and LV4, however, the
181 distribution of scores was broad among resampling replicates and mostly indistinguishable from
182 zero (Supplementary Fig. S2). Uncertainty in the trailing LVs may stem from model iterations
183 requiring less than 4 LVs to explain the variance in that iteration. The analysis further supports
184 that the lagging LVs of this model do not contain prevailing trends in the data but instead capture
185 a specific replicate configuration of the animals used.

186

187 *Data pairing does not significantly alter results of nested resampling*

188 In the Bersi *et al.*³⁹ study, inbred animals sacrificed at several time points were doubly used
189 to collect enzymatic–cellular histology (\underline{X}) and mechanical data (\underline{Y} ; Fig. 1). Possibly, the paired
190 animal-by-animal covariation of histology and mechanics was greater than the condition-wide
191 averages. We sought to evaluate the relative importance of within-animal pairing between
192 independent and dependent datasets by applying nested resampling. To do so, we built a second
193 PLSR model using only the time points with paired enzymatic–cellular and mechanical data: 0,
194 4, 14, and 28 days (Fig. 2). For the second model, resampling was coupled between \underline{X} and \underline{Y} to
195 retain the paired information of each animal selected by bootstrapping. The interpretation of

196 bootstrap-resampled time weights for the paired model was then compared with the original
197 unpaired model to determine if conclusions were fundamentally different.

198 We found that the LV1–LV2 time weights obtained by paired sampling were
199 indistinguishable from those obtained by unpaired sampling (Fig. 5, upper). Relative to their
200 corresponding global-average model, both analyses indicated that the dynamics associated with
201 LV1 and LV2 were robust, consistent with the prior assessment of mechanical weights for these
202 LVs (Fig. 4). Histological time weights were similarly reliable for LV3 and LV4, but mechanical
203 time weights were highly variable and largely overlapping with zero (Fig. 5, lower). No
204 statistically significant differences were identified between paired and unpaired time weights in
205 LV3 or LV4 ($p > 0.25$ following two-way ANOVA with Tukey’s post-hoc test for differences
206 between paired–unpaired or independent–dependent time weights), indicating that pairing does
207 not add statistical power to the trailing LVs for this dataset. More generally, the analysis suggests
208 that unpaired *in vivo* designs may be sufficient for nested resampling to assess the stability of
209 model components.

210

211 *Generality of nested resampling to other multidimensional in vivo and in vitro datasets*

212 The LV fragilities revealed by nested resampling could be specific to the Bersi *et al.*³⁹
213 dataset. We thus sought another *in vivo* study comprised of multiple molecular–cellular
214 measurements, time points, and animals where nested replicate information could be recovered
215 confidently. Raw data was obtained from Lau *et al.*¹⁴, who examined the molecular and cellular
216 inflammatory response of the small intestine to the cytokine tumor necrosis factor α (TNF α).
217 Animals ($N = 5$) were administered one of two doses of TNF α and sacrificed at one of six time
218 points after administration. From each animal, two intestinal regions were analyzed for signaling

219 by Luminex phosphoproteomics, cell proliferation by immunohistochemistry, and overall cell
220 death by western blotting (Table 2). The data were used previously to classify cell-fate
221 responses¹⁴—we asked here whether cell proliferation and death were predicted quantitatively
222 from the time-resolved phosphoproteomic observations. If so, then nested resampling could
223 address how robust or fragile those predictions were to the animals included.

224 We organized and standardized the data (Supplementary Fig. S3), building a single PLSR
225 model of the global averages along with 500 null models by randomization. For the Lau *et al.*¹⁴
226 dataset, a three-LV model was optimal and yielded good predictive accuracy (Fig. 6). LV1 of the
227 global-average model did not discriminate between tissues or outcomes, but LV2 separated cell
228 proliferation (ph3) vs. death (cc3) readouts and LV3 stratified duodenal vs. ileal segments of the
229 intestine (Supplementary Fig. S4). Furthermore, randomization suggested that the ph3–cc3
230 distinction along LV2 was far outside chance expectation (Fig. 7a, left). Nested resampling,
231 however, revealed a pronounced fragility of output weights when accounting for inter-replicate
232 variability. Both jackknifing and bootstrapping eliminated any discrimination along LV2 (Fig. 7a,
233 middle and right), undermining model interpretations based on it. Similarly, the time-dependent
234 behavior associated with LV2 and LV3 (Fig. 7b) mostly reverted to near zero after bootstrap
235 resampling (Fig. 7c). Therefore, as with the Bersi *et al.*³⁹ study, the lagging components of this
236 multidimensional PLSR model capture *in vivo* replicate instabilities instead of salient trends in the
237 data.

238 It is possible that nested resampling excludes lagging LVs in any multidimensional dataset
239 irrespective of its origin. To determine if fragility is tied to the higher biological variability of *in*
240 *vivo* datasets, we reassessed an earlier multidimensional PLSR model built from global averages
241 of *in vitro* measurements. The model of Chitforoushzadeh *et al.*¹³ predicts gene-expression cluster

242 dynamics from intracellular signaling in a colon-cancer cell line stimulated with combinations of
243 cytokines and growth factors^{3,35,44}. Cell extracts ($N = 2-6$) were collected at three or 13 time points
244 and measured transcriptomically by microarray or for signaling by various methods (Table 3). The
245 prior hypothesis was that quantitative predictions of gene-expression dynamics would uncover
246 novel upstream signaling regulators of transcriptional programs¹³.

247 After obtaining the original dataset and confirming the nested replicate structure, we
248 modeled the mean dataset (Supplementary Fig. S5) standardized as before¹³. The global-average
249 model was optimally decomposed with four LVs, and randomizing 500 null models reproduced
250 all the meaningfully weighted parameters (*e.g.*, gene-cluster weights) described in the original
251 study (Fig. 8a,b). Remarkably, when nested resampling was applied to this PLSR model, the
252 conclusions were largely unaltered. Cluster weights were retained in ~90% of LV2 and LV3 and
253 even ~56% of LV4 (Fig. 8c-f), bolstering prior interpretations of this PLSR model along with
254 others built upon highly reproducible *in vitro* data^{3-9,13}.

255 Using all three models resampled here, we plotted RMSE as a function of increasing LV
256 for the global-average model compared to its mean jackknife or bootstrap replication. For the
257 Chitforoushzadeh *et al.*¹³ model built from *in vitro* data, jackknife and bootstrap resamplings were
258 superimposable with the global average (Fig. 9a). However, for the two *in vivo* studies, the
259 resampled variants were consistently less accurate than the corresponding global average (Fig.
260 9b,c). Taken together, the results indicate that nested resampling is an effective strategy—distinct
261 from prevailing methods—to benchmark meaningful LVs extracted from *in vivo* datasets.

262

263 DISCUSSION

264 When applied to *in vivo* PLSR models, nested resampling is an effective way to hone in on
265 latent variables that are robust to the replicate fluctuations of individual inbred animals. For high-
266 variance observations, the method gives information complementary to that obtained by condition-
267 specific jackknifing³⁸ or crossvalidation¹⁰. In building hundreds of instances around the global-
268 average model, nested resampling does not rely on any further assumptions to execute. However,
269 it is important to recognize the nesting relationships within a study design and ensure that they are
270 retained during resampling. The diversity of study designs³³ precludes a universal software for
271 nested resampling, but we provide code for the specific implementations here, which can readily
272 be adapted for other *in vivo* datasets (Supplementary File S1).

273 Normally, direct use of replicated data in PLSR is discouraged, because replicates inflate
274 the number of observations and reduce the stringency of crossvalidation³². Resampling avoids data
275 inflation but is minimally effective for latent-variable assessment when replicates are highly
276 reproducible. The *in vitro* model¹³ resampled here uses data with a median coefficient of variation
277 of ~11% (Ref. ⁴⁴), which is too small to impact the latent variables of the model. In mice, however,
278 phenotypic variability within inbred strains is typically 3–5 times greater³¹, competing with the
279 biological effect size of many studies. Replicates are essential for more reliable central estimates
280 and statistical power⁴⁵. This work shows how replicates can be repurposed to reflect better the
281 internal variability of *in vivo* datasets and identify the robust vs. fragile components of regression
282 models that are ordinarily limited to using replication indirectly.

283 The *in vivo* datasets modeled here used inbred strains of mice to minimize genotypic
284 differences. Modeling outbred strains of animals³¹ or diverse human populations⁴⁶ will involve
285 very different approaches. Rather than averaging (followed by jackknife–bootstrap resampling),
286 each individual will be better handled as a separate observation if the independent and dependent

287 data can be reliably paired to that individual. Data pairing may be particularly difficult when \underline{X}
288 and \underline{Y} observations are collected at multiple time points. The paired-vs.-unpaired resampling
289 comparison involving the Bersi *et al.*³⁹ dataset (Fig. 5) provides a useful guide for determining
290 when less conservative experimental designs (*i.e.*, averaging without pairing) are acceptable.

291 The nested methods proposed here differ from prior resampling approaches that focus on
292 defining observation sets for proper model selection⁴⁷. Numerical Monte-Carlo simulations have
293 a rich history in PLSR originating in chemometrics^{48,49}. However, applications to replicated data
294 have not been considered previously, likely because of the high reproducibility of measured
295 chemical spectra. In nested resampling, the bootstrap and jackknife gauge different ends of latent-
296 variable robustness. Bootstrapping is highly conservative, evaluating whether any random draw of
297 replicates yields essentially the same model. Latent variables that survive bootstrapping capture
298 large, reproducible effect sizes and thus are highly robust. Conversely, jackknifing is a much
299 weaker test of model fragility. Global-average relationships that disappear with jackknifing are
300 severely underpowered and should be ignored or followed up with more replicates. Together, these
301 established tools from computational statistics³⁴ enable formal examination of data qualities that
302 would otherwise be inaccessible by PLSR alone.

303 The concepts put forth here generalize to other data-driven approaches besides PLSR. For
304 example, when classifying observations by support vector machines⁵⁰, the handling of replicated
305 observations is often heuristic. Heinemann *et al.*⁵¹ investigated the effects of replicate
306 downsampling on classification by metabolomics data with small or large variance, but nesting of
307 replicates within observations was not considered as we did. Nested resampling of PLSR models
308 shares conceptual analogies with the method of random forests⁵² for decision tree classifiers.
309 Individual decision trees are unstable in their predictions, but robustness is improved when training

310 data are randomly resampled to make ensemble classifications. Biological data *in vivo* are typically
311 noisy and the number of observations is often limited, suggesting that some form of nested
312 resampling would be beneficial for many data-driven methods seeking to identify molecular–
313 cellular drivers of organismal phenotypes.

314 A primary motivation for applying PLSR in biological systems is to simplify complex
315 observations and generate testable hypotheses^{2,36}. The latter goal is impossible when chasing latent
316 variables that are statistically significant overall but fragile upon replication. By using all of the *in*
317 *vivo* data available, nested resampling identifies where PLSR stops modeling effect sizes and starts
318 fitting biologically noisy averages. It contributes to the ongoing effort to improve the
319 reproducibility of models⁵³ and preclinical research^{26,54}.

320

321 **MATERIALS AND METHODS**

322 *Experimental models*

323 Three studies were selected in which an inflammatory agent was administered *in vivo* or *in*
324 *vitro* and subsequent temporal and/or spatial analyses were performed^{13,14,39}. First, source data
325 were obtained from Bersi *et al.*³⁹ in which male *ApoE*^{-/-} mice were infused with Angiotensin II
326 (AngII, 1000 ng/kg/min) via an implantable osmotic mini-pump for 4, 7, 14, 21, or 28 days.
327 Following treatment, the aorta was harvested and separated into four regions: 1) the ascending
328 thoracic aorta (ATA) spanning from the aortic root to the brachiocephalic artery, 2) the descending
329 thoracic aorta (DTA) spanning from the left subclavian artery to the 4th or 5th pair of intercostal
330 arteries, 3) the suprarenal abdominal aorta (SAA) spanning from the diaphragm to the left renal
331 artery, and 4) the infrarenal abdominal aorta (IAA) spanning from the left renal artery to the iliac
332 trifurcation. Vessels were cleaned, sutured, and mounted on an opposing glass cannula and

333 subjected to passive biomechanical testing without contribution from smooth muscle as previously
334 described⁵⁵. Briefly, vessels were preconditioned to minimize viscoelastic behavior of the material
335 and then subjected to three fixed-length, pressure-diameter inflation tests and four fixed-pressure,
336 force-length extension tests. Following testing, vessels were fixed in 10% neutral buffered
337 formalin, embedded in paraffin, and sectioned and stained with Movat's pentachrome, Picrosirius
338 red, or Elastica van Gieson to quantify layer-specific matrix content. Additional slides were stained
339 for CD3, CD45, CD68, MMP2, MMP12, or MMP13 expression. Details regarding region- and
340 layer-specific matrix, inflammatory cell, and enzyme content can be found in the original
341 publication³⁹. Animal housing and experimental procedures were carried out in compliance with
342 regulations and protocols approved by the Institutional Animal Care and Use Committee at Yale
343 University.

344 Passive mechanical properties of the tissue were quantified using a microstructurally-
345 motivated strain energy function assuming hyperelasticity. The analytical methods for determining
346 mechanical metrics have been described in detail previously⁵⁵. Briefly, biaxial Cauchy wall
347 stresses were calculated as

$$348 \quad \mathbf{t} = -p\mathbf{I} + 2\mathbf{F}\frac{\partial W}{\partial \mathbf{C}}\mathbf{F}^T \quad (1)$$

349 where \mathbf{t} is the Cauchy stress tensor, p is the Lagrange multiplier enforcing incompressibility, \mathbf{I} is
350 the second-order identity matrix, \mathbf{F} is the deformation gradient mapping spatial coordinates from
351 a reference to deformed configuration, \mathbf{C} is the right Cauchy-Green deformation tensor ($\mathbf{C} = \mathbf{F}^T\mathbf{F}$),
352 and W is a microstructurally-motivated strain energy density function reflecting contributions of
353 matrix constituents to material behavior. Linearized biaxial material stiffnesses were determined
354 in terms of the second derivative of W with respect to deformations. These metrics, along with

355 associated loaded geometry, were evaluated at group-specific blood pressures and at estimated *in*
356 *vivo* axial stretch values.

357 For the second study, source data were obtained from Lau *et al.*¹⁴ in which male C57BL/6J
358 mice were injected with 5 or 10 μg TNF α by retro-orbital injection for 0.5, 1, 2, 4, or 8 hours.
359 Following treatment, mice were euthanized, and two regions of the small intestine were harvested:
360 1) the duodenum consisting of the 1 cm of area immediately distal to the stomach, and 2) the ileum
361 consisting of the 3 cm of area immediately proximal to the cecum. Tissue samples were rinsed in
362 PBS and lysed and homogenized in Bio-Plex lysis buffer or fixed in formalin for
363 immunohistochemical analysis. Data characterizing apoptosis and proliferation were obtained by
364 quantitative immunoblotting for cleaved caspase 3 (cc3) and by immunohistochemistry for
365 phosphorylated histone 3 (ph3), respectively. Signaling data were obtained via Bio-Plex signaling
366 analysis. The targets included pI κ B α , pJnk, pMek1, pErk1/2, pRsk, pp38, pc-Jun, pAtf2, pAkt,
367 pS6, pStat3, and Mek1, totaling 12 signaling targets. Details regarding the quantification of
368 apoptosis, proliferation, and signaling are in the original publication¹⁴. Animal housing and
369 experimental procedures were carried out in compliance with regulations and protocols approved
370 by the Subcommittee on Research Animal Care at Massachusetts General Hospital.

371 For the third study, source data were obtained from Chitforoushzadeh *et al.*¹³ in which HT-
372 29 cells were pretreated with interferon γ (IFN γ ; 200 U/mL) for 24 hours and subsequently treated
373 with various combinations and concentrations of TNF α , insulin, and epidermal growth factor
374 (EGF) for 5 min, 15 min, 30 min, 1 hours, 1.5 hours, 2 hours, 4 hours, 8 hours, 12 hours, 16 hours,
375 20 hours, or 24 hours. Signaling metrics included 12 proteins that were evaluated via kinase
376 activity, protein phosphorylation, total protein, phospho-total ratio, zymogen amount, or cleaved
377 amount. Proteins included ERK, Akt, JNK1, IKK, MK2, pMEK, pFKHR, pIRS1, caspase 8,

378 caspase 3, and EGFR. The combination of 12 proteins and multiple possible proteoforms (*e.g.*,
379 phosphorylated protein and total protein) yielded a total of 19 signaling metrics. Additionally,
380 microarray profiling of HT-29 cells was performed on Affymetrix U133A arrays and organized
381 by Cluster Identification via Connectivity Kernels (CLICK). Briefly, cells were pretreated with
382 IFN γ (200 U/mL) for 24 hours before stimulation with TNF α (0, 5, or 100 ng/mL), insulin (0, 5,
383 or 500 ng/mL), and EGF (0, 1, or 100 ng/mL) for 4, 8, or 16 hours. CLICK clustering of microarray
384 data yielded 9 clusters for each condition and time point¹³.

385 For all studies, global averages were calculated as the mean among replicates.

386

387 *Multidimensional partial least squares modeling*

388 Multidimensional PLSR was performed in MATLAB using version 2.02 of the NPLS
389 Toolbox⁵⁶ after dividing each study into independent and dependent datasets according to the
390 stated hypothesis. Model variables for the three studies are listed in Tables 1–3 with associated
391 abbreviations, methods of acquisition, sample sizes, and input–output classifications. The
392 algorithm for PLSR has been described in detail previously with specific application to multi-
393 linear frameworks^{13,57}. Briefly, PLSR is a simultaneous decomposition of two matrices where the
394 scores of each decomposition are linearly related (Fig. 1). Various options exist for exact
395 algorithms. The algorithm applied in this study is detailed below:

396 1) Organize independent data into an $i \times j \times k$ array \mathbf{X} , where i is the number of experimental
397 conditions, j is the number of time points, and k is the number of variables in the
398 independent dataset. In parallel, organize the dependent data into an $i \times l \times m$ array \mathbf{Y} where
399 l is the number of time points, and m is the number of variables in the dependent dataset.

400 Note that the algorithm requires the first dimension of each matrix to be equal but numbers
401 of variables and time points need not be equal.

402 2) Standardize the data by mean centering and/or variance scaling the data. Different
403 standardization techniques can yield markedly different results⁵⁸. For Bersi *et al.*³⁹, only
404 variance scaling across mode 3 was performed, and time 0 values were subtracted for a
405 given condition and variable from all other corresponding time points within the same
406 condition and variable such that regional differences are not considered at baseline. For
407 Lau *et al.*¹⁴ and Chitforoushzadeh *et al.*¹³, variance scaling across modes 2 and 3 was
408 performed.

409 3) Initialize an $i \times 1$ vector for the n^{th} latent variable for the dependent condition scores, \mathbf{u} ,
410 and the independent condition scores, \mathbf{t} . Here, \mathbf{u} is initialized by performing principal
411 components analysis on the standardized residual \mathbf{X} matrix (which equals the original
412 scaled \mathbf{Y} matrix for the first LV) and setting \mathbf{u} = principal component 1. The vector \mathbf{t} is
413 randomly initialized.

414 4) Calculate variable and time weights for the independent data, \mathbf{w} , by back projecting the
415 independent data, \mathbf{X} , onto \mathbf{u} ,

$$416 \quad \mathbf{w} = \mathbf{X}^T \mathbf{u} \quad (3)$$

417 Back projection requires unfolding \mathbf{X} into an $i \times (j*k)$ matrix, \mathbf{X} .

418 5) Update independent condition scores, \mathbf{t} , by projecting \mathbf{X} onto \mathbf{w} ,

$$419 \quad \mathbf{t} = \mathbf{Xw} \quad (4)$$

420 6) Calculate variable and time weights for the dependent data, \mathbf{q} , by back projecting the
421 residual of the \mathbf{Y} matrix onto \mathbf{t} ,

$$422 \quad \mathbf{q} = \mathbf{Y}^T \mathbf{t} \quad (5)$$

423 Back projection requires unfolding \mathbf{X} into an $i \times (l \times m)$ matrix, \mathbf{Y} .

424 7) Update dependent condition scores, \mathbf{u} , by projecting the residual of \mathbf{Y} onto \mathbf{q} ,

$$425 \quad \mathbf{u} = \mathbf{Y}\mathbf{q} \quad (6)$$

426 8) Calculate the difference in magnitude between the updated \mathbf{t} from step 5 and the original \mathbf{t}
427 from step 3 (or the previously calculated \mathbf{t} if on iteration 2 or more) and return to step 4 as
428 long as the change in magnitude remains above a critical threshold (here, 10^{-10}).

429 9) Calculate the regression coefficient between the independent and dependent condition
430 scores,

$$431 \quad \mathbf{B} = (\mathbf{T}^T\mathbf{T})^{-1}\mathbf{T}^T\mathbf{U} \quad (7)$$

432 where \mathbf{B} is an $n \times n$ matrix where n is the number of the current LV. If the calculation is
433 for the first LV, then \mathbf{B} becomes a scalar calculated as $b = (\mathbf{t}^T\mathbf{t})^{-1}\mathbf{t}^T\mathbf{u}$.

434 10) Calculate the residuals of \mathbf{X} and \mathbf{Y} by subtracting the decomposed matrices from the
435 previous residual matrices.

436 11) Complete steps 4 – 10 for the desired number of LVs using \mathbf{X} and \mathbf{Y}_{res} .

437 Statistical significance of variable weights was determined by calculating a null PLSR
438 model in which raw data were shuffled within mode 1 (*i.e.*, time and variable data were shuffled
439 within each condition) and re-standardized, and the scores and weights recalculated according to
440 the previously mentioned algorithm. Average scores and weights were calculated for 500 iterations
441 of reshuffling, and meaningful scores–weights were considered to be those exceeding one standard
442 deviation from the mean. The PLSR model was cross-validated using a leave-one-out approach in
443 which predictions for one condition are calculated from parameters derived from the remaining
444 conditions. The root mean squared error (RMSE) for the cross-validated predictions was calculated

445 with the addition of each LV, and the optimal number of LVs was determined by the number of
446 LVs that minimized the RMSE in the global-average model.

447

448 *Nested resampling*

449 Data subsets were generated by sampling individual replicates for each condition and time
450 point by using a jackknifing (leave-one-out) approach or bootstrapping (leave-one-in) approach,
451 and PLSR models were developed for each sampled dataset. Data were resampled 500 times with
452 or without retention of data pairing by animal if pairing information was available. Replicate sizes
453 per condition per time point are denoted in Tables 1–3. From Bersi *et al.*³⁹, the majority of the
454 histological samples were paired to one of the biomechanical datasets and were chosen based on
455 the nearness of the unloaded thickness to the mean within each condition (aortic region) and time
456 point. For ph3 data in Lau *et al.*¹⁴, source data for individual replicates was not available because
457 of blinding in the original study. Therefore, sets of 5 individual samples for each condition
458 (intestinal region and TNF α dose) and time point were simulated from published means and
459 standard deviations by assuming the data were normally distributed.

460 For each randomly generated dataset, scores and weights were calculated using the number
461 of LVs required for the corresponding mean dataset to facilitate comparison to the global-average
462 model. Each model was cross-validated using the leave-one-out approach as previously described,
463 and scores, weights, and cross-validated predictions were summarized and compared to the
464 corresponding values derived from the model of the mean dataset.

465

466 REFERENCES

- 467 1. Albeck, J. G. *et al.* Collecting and organizing systematic sets of protein data. *Nat. Rev. Mol.*
468 *Cell Biol.* **7**, 803 (2006).
- 469 2. Janes, K. A. & Yaffe, M. B. Data-driven modelling of signal-transduction networks. *Nat.*
470 *Rev. Mol. Cell Biol.* **7**, 820–828 (2006).
- 471 3. Janes, K. A. *et al.* A systems model of signaling identifies a molecular basis set for cytokine-
472 induced apoptosis. *Science* **310**, 1646–1653 (2005).
- 473 4. Niepel, M. *et al.* Profiles of basal and stimulated receptor signaling networks predict drug
474 response in breast cancer lines. *Sci. Signal.* **6**, ra84–ra84 (2013).
- 475 5. Fallahi-Sichani, M. *et al.* Systematic analysis of BRAFV600E melanomas reveals a role for
476 JNK/c-Jun pathway in adaptive resistance to drug-induced apoptosis. *Mol. Syst. Biol.* **11**, 797
477 (2015).
- 478 6. Lee, M. J. *et al.* Sequential application of anticancer drugs enhances cell death by rewiring
479 apoptotic signaling networks. *Cell* **149**, 780–794 (2012).
- 480 7. Miller-Jensen, K., Janes, K. A., Brugge, J. S. & Lauffenburger, D. A. Common effector
481 processing mediates cell-specific responses to stimuli. *Nature* **448**, 604–608 (2007).
- 482 8. Tentner, A. R. *et al.* Combined experimental and computational analysis of DNA damage
483 signaling reveals context-dependent roles for Erk in apoptosis and G1/S arrest after
484 genotoxic stress. *Mol. Syst. Biol.* **8**, 568 (2012).
- 485 9. Jensen, K. J. *et al.* An ERK-p38 subnetwork coordinates host cell apoptosis and necrosis
486 during coxsackievirus B3 infection. *Cell Host Microbe* **13**, 67–76 (2013).
- 487 10. Geladi, P. & Kowalski, B. R. Partial least-squares regression: a tutorial. *Anal. Chim. Acta*
488 **185**, 1–17 (1986).

- 489 11. Dworkin M., Mukherjee S., Jayaprakash C. & Das J. Dramatic reduction of dimensionality
490 in large biochemical networks owing to strong pair correlations. *J. Royal Soc. Interface* **9**,
491 1824–1835 (2012).
- 492 12. Janes, K. A., Reinhardt, H. C. & Yaffe, M. B. Cytokine-induced signaling networks
493 prioritize dynamic range over signal strength. *Cell* **135**, 343–354 (2008).
- 494 13. Chitforoushzadeh, Z. *et al.* TNF-insulin crosstalk at the transcription factor GATA6 is
495 revealed by a model that links signaling and transcriptomic data tensors. *Sci. Signal.* **9**, ra59–
496 ra59 (2016).
- 497 14. Lau, K. S. *et al.* In vivo systems analysis identifies spatial and temporal aspects of the
498 modulation of TNF- α -induced apoptosis and proliferation by MAPKs. *Sci. Signal.* **4**, ra16–
499 ra16 (2011).
- 500 15. Lau, K. S. *et al.* Multi-scale in vivo systems analysis reveals the influence of immune cells
501 on TNF- α -induced apoptosis in the intestinal epithelium. *PLOS Biol.* **10**, e1001393 (2012).
- 502 16. Arnold, K. B., Szeto, G. L., Alter, G., Irvine, D. J. & Lauffenburger, D. A. CD4⁺ T cell–
503 dependent and CD4⁺ T cell-independent cytokine-chemokine network changes in the
504 immune responses of HIV-infected individuals. *Sci. Signal.* **8**, ra104–ra104 (2015).
- 505 17. Chung, A. W. *et al.* Dissecting polyclonal vaccine-induced humoral immunity against HIV
506 using systems serology. *Cell* **163**, 988–998 (2015).
- 507 18. Prim, D. A. *et al.* Comparative mechanics of diverse mammalian carotid arteries. *PLOS ONE*
508 **13**, e0202123 (2018).
- 509 19. Shadwick, R. E. Mechanical design in arteries. *J. Exp. Biol.* **202**, 3305–3313 (1999).

- 510 20. Bersi, M. R., Ferruzzi, J., Eberth, J. F., Jr, R. L. G. & Humphrey, J. D. Consistent
511 biomechanical phenotyping of common carotid arteries from seven genetic,
512 pharmacological, and surgical mouse models. *Ann. Biomed. Eng.* **42**, 1207–1223 (2014).
- 513 21. Bellini, C. *et al.* Comparison of 10 murine models reveals a distinct biomechanical
514 phenotype in thoracic aortic aneurysms. *J. Royal Soc. Interface* **14**, 20161036 (2017).
- 515 22. Ramachandra, A. B. & Humphrey, J. D. Biomechanical characterization of murine
516 pulmonary arteries. *J. Biomech. Eng.* (2018). doi:10.1016/j.jbiomech.2018.12.012
- 517 23. Kobs, R. W., Muvarak, N. E., Eickhoff, J. C. & Chesler, N. C. Linked mechanical and
518 biological aspects of remodeling in mouse pulmonary arteries with hypoxia-induced
519 hypertension. *Am. J. Physiol. Heart Circ. Physiol.* **288**, H1209–H1217 (2005).
- 520 24. Ferruzzi, J., Bersi, M. R., Uman, S., Yanagisawa, H. & Humphrey, J. D. Decreased elastic
521 energy storage, not increased material stiffness, characterizes central artery dysfunction in
522 fibulin-5 deficiency independent of sex. *J. Biomech. Eng.* **137**, 031007–031007 (2015).
- 523 25. Wan, W., Yanagisawa, H. & Jr, R. L. G. Biomechanical and microstructural properties of
524 common carotid arteries from fibulin-5 null mice. *Ann. Biomed. Eng.* **38**, 3605–3617 (2010).
- 525 26. Nosek, B. A. & Errington, T. M. Making sense of replications. *eLife* **6**, e23383 (2017).
- 526 27. Golob, M. J. *et al.* Cardiovascular function and structure are preserved despite induced
527 ablation of BMP1-related proteinases. *Cel. Mol. Bioeng.* **11**, 255–266 (2018).
- 528 28. Cadwell, K. *et al.* Virus-plus-susceptibility gene interaction determines Crohn’s Disease
529 gene Atg16L1 phenotypes in intestine. *Cell* **141**, 1135–1145 (2010).
- 530 29. Korneva, A. & Humphrey, J. D. Maladaptive aortic remodeling in hypertension associates
531 with dysfunctional smooth muscle contractility. *Am. J. Physiol. Heart Circ. Physiol.* **316**,
532 H265–H278 (2018).

- 533 30. Hildebrand, F. *et al.* Inflammation-associated enterotypes, host genotype, cage and inter-
534 individual effects drive gut microbiota variation in common laboratory mice. *Genome Biol.*
535 **14**, R4 (2013).
- 536 31. Tuttle, A. H., Philip, V. M., Chesler, E. J. & Mogil, J. S. Comparing phenotypic variation
537 between inbred and outbred mice. *Nat. Methods* **15**, 994 (2018).
- 538 32. Martens, H. & Martens, M. Multivariate analysis of quality. An introduction. *Meas. Sci.*
539 *Technol.* **12**, 1746–1746 (2001).
- 540 33. Krzywinski, M., Altman, N. & Blainey, P. Points of significance: Nested designs. *Nat.*
541 *Methods* **11**, 977–978 (2014).
- 542 34. Efron, B. & Tibshirani, R. J. *An introduction to the bootstrap.* (CRC Press, 1994).
- 543 35. Gaudet, S. *et al.* A compendium of signals and responses triggered by prodeath and
544 prosurvival cytokines. *Mol. Cell Proteomics* **4**, 1569–1590 (2005).
- 545 36. Jensen, K. J. & Janes, K. A. Modeling the latent dimensions of multivariate signaling
546 datasets. *Phys. Biol.* **9**, 045004 (2012).
- 547 37. Halabi, N., Rivoire, O., Leibler, S. & Ranganathan, R. Protein sectors: Evolutionary units of
548 three-dimensional structure. *Cell* **138**, 774–786 (2009).
- 549 38. Westad, F. & Martens, H. Variable selection in near infrared spectroscopy based on
550 significance testing in partial least squares regression. *J. Near Infrared Spectrosc.* **8**, 117–
551 124 (2000).
- 552 39. Bersi, M. R., Khosravi, R., Wujciak, A. J., Harrison, D. G. & Humphrey, J. D. Differential
553 cell-matrix mechanoadaptations and inflammation drive regional propensities to aortic
554 fibrosis, aneurysm or dissection in hypertension. *J. Royal Soc. Interface* **14**, 20170327
555 (2017).

- 556 40. Daugherty, A., Manning, M. W. & Cassis, L. A. Angiotensin II promotes atherosclerotic
557 lesions and aneurysms in apolipoprotein E-deficient mice. *J. Clin. Invest.* **105**, 1605–1612
558 (2000).
- 559 41. Bro, R. Multiway calibration. Multilinear PLS. *J. Chemom.* **10**, 47–61 (1996).
- 560 42. Goldfinger, J. Z. *et al.* Thoracic aortic aneurysm and dissection. *J. Am. Coll. Cardiol.* **64**,
561 1725–1739 (2014).
- 562 43. Mattace-Raso, F. U. *et al.* Arterial stiffness and risk of coronary heart disease and stroke: the
563 Rotterdam Study. *Circulation* **113**, 657–663 (2006).
- 564 44. Janes, K. A. *et al.* The response of human epithelial cells to TNF involves an inducible
565 autocrine cascade. *Cell* **124**, 1225–1239 (2006).
- 566 45. Krzywinski, M. & Altman, N. Points of significance: Power and sample size. *Nat. Methods*
567 **10**, 1139–1140 (2013).
- 568 46. Guyatt, G. H. The n-of-1 randomized controlled trial: Clinical usefulness: Our three-year
569 experience. *Ann. Intern. Med.* **112**, 293 (1990).
- 570 47. Kvalheim, O. M., Grung, B. & Rajalahti, T. Number of components and prediction error in
571 partial least squares regression determined by Monte Carlo resampling strategies. *Chemom.*
572 *Intell. Lab. Syst.* **188**, 79–86 (2019).
- 573 48. Martens, H. A. & Dardenne, P. Validation and verification of regression in small data sets.
574 *Chemom. Intell. Lab. Syst.* **44**, 99–121 (1998).
- 575 49. Geladi, P. & Kowalski, B. R. An example of 2-block predictive partial least-squares
576 regression with simulated data. *Anal. Chim. Acta* **185**, 19–32 (1986).
- 577 50. Noble, W. S. What is a support vector machine? *Nat. Biotechnol.* **24**, 1565 (2006).

- 578 51. Heinemann, J., Mazurie, A., Tokmina-Lukaszewska, M., Beilman, G. J. & Bothner, B.
579 Application of support vector machines to metabolomics experiments with limited replicates.
580 *Metabolomics* **10**, 1121–1128 (2014).
- 581 52. Breiman, L. Random forests. *Mach. Learn.* **45**, 5–32 (2001).
- 582 53. Medley, J. K., Goldberg, A. P. & Karr, J. R. Guidelines for reproducibly building and
583 simulating systems biology models. *IEEE Trans. Biomed. Eng.* **63**, 2015–2020 (2016).
- 584 54. Begley, C. G. & Ellis, L. M. Drug development: Raise standards for preclinical cancer
585 research. *Nature* **483**, 531–533 (2012).
- 586 55. Ferruzzi, J., Bersi, M. R. & Humphrey, J. D. Biomechanical phenotyping of central arteries
587 in health and disease: Advantages of and methods for murine models. *Ann. Biomed. Eng.* **41**,
588 1311–1330 (2013).
- 589 56. Andersson, C. A. & Bro, R. The N-way toolbox for MATLAB. *Chemom. Intell. Lab. Syst.*
590 **52**, 1–4 (2000).
- 591 57. Wold, S., Geladi, P., Esbensen, K. & Öhman, J. Multi-way principal components-and PLS-
592 analysis. *J. Chemom.* **1**, 41–56 (1987).
- 593 58. Bro, R. & Smilde, A. K. Centering and scaling in component analysis. *J. Chemom.* **17**, 16–33
594 (2003).
- 595
- 596
- 597
- 598

599 **ACKNOWLEDGEMENTS**

600 The authors would like to thank Dr. Matthew Bersi and Prof. Ken Lau for generously providing
601 source data and the interpretations needed for its reuse in this study and Prof. Jay Humphrey for
602 his valuable insight and feedback during the study design and manuscript preparation. This work
603 was supported by the David & Lucile Packard Foundation #2009-34710 (K.A.J.) and the National
604 Institutes of Health #U01-CA215794 (K.A.J.) and #R01-HL105297 (C.A. Figueroa and J.D.
605 Humphrey).

606

607 **COMPETING INTERESTS STATEMENT**

608 The authors declare no competing interests.

609

610 **AUTHOR CONTRIBUTIONS**

611 A.W.C. participated in study design, code generation, model development and
612 interpretation, and manuscript preparation. K.A.J. led the study design and participated in model
613 interpretation and manuscript preparation. Both authors reviewed and approved the manuscript.

614

615 **DATA AVAILABILITY**

616 All code and source data are available in Supplementary File S1. Parameter values for the
617 the Bersi *et al.*³⁹, Lau *et al.*¹⁴, and Chitforoushzadeh *et al.*¹³ PLSR models are available in
618 Supplementary File S2.

619 TABLES AND FIGURES

620 **Table 1.** Symbols, metrics, methods of acquisition, and sample sizes per condition per time point
 621 ($N =$) for the PLSR model of Bersi *et al.*³⁹. Histological stains used for matrix quantification
 622 include Elastica van Gieson (elastin – black stain), Movat’s Pentachrome (smooth muscle cells –
 623 red stain, GAGs – blue stain), and Picrosirius Red (collagen). Output samples were whole aortic
 624 sections from one mouse which were formalin-fixed after testing. Input samples were slides from
 625 output samples chosen for sectioning and staining based on their proximity to the mean thickness
 626 of their associated groups. Inputs were averages of three sections per slide.

<i>Symbol</i>	<i>Variable Name (Mode 3)</i>	<i>Method</i>	<i>N =</i>	<i>Input/Output</i>
eln ^m	Elastin - media	Histology	2	Input
col ^m	Collagen - media	Histology	2	Input
SMC ^m	Smooth muscle cells - media	Histology	2	Input
GAG ^m	Glycosaminoglycans - media	Histology	2	Input
col ^a	Collagen - adventitia	Histology	2	Input
CD3 ^m	Cluster of differentiation 3 - media	Immunofluorescence	2	Input
CD45 ^m	Cluster of differentiation 45 - media	Immunofluorescence	2	Input
CD68 ^m	Cluster of differentiation 68 - media	Immunofluorescence	2	Input
CD3 ^a	Cluster of differentiation 3 - adventitia	Immunofluorescence	2	Input
CD45 ^a	Cluster of differentiation 45 - adventitia	Immunofluorescence	2	Input
CD68 ^a	Cluster of differentiation 68 - adventitia	Immunofluorescence	2	Input
MMP2 ^m	Matrix metalloproteinase 2 - media	Immunofluorescence	2	Input
MMP12 ^m	Matrix metalloproteinase 12 - media	Immunofluorescence	2	Input
MMP13 ^m	Matrix metalloproteinase 13 - media	Immunofluorescence	2	Input
MMP2 ^a	Matrix metalloproteinase 2 - adventitia	Immunofluorescence	2	Input
MMP12 ^a	Matrix metalloproteinase 12 - adventitia	Immunofluorescence	2	Input
MMP13 ^a	Matrix metalloproteinase 13 - adventitia	Immunofluorescence	2	Input
OD	Unloaded outer diameter	Biaxial testing	4 - 7	Output
H	Unloaded thickness	Imaging	4 - 7	Output
od	Systolic outer diameter	Biaxial testing	4 - 7	Output
h	Systolic thickness	Biaxial testing	4 - 7	Output
ir	Systolic inner radius	Biaxial testing	4 - 7	Output
$\lambda_{z,iv}$	<i>In vivo</i> axial stretch	Biaxial testing	4 - 7	Output
$\sigma_{\theta\theta}$	Circumferential stress	Biaxial testing	4 - 7	Output
σ_{zz}	Axial stress	Biaxial testing	4 - 7	Output
$C_{\theta\theta\theta\theta}$	Circumferential stiffness	Biaxial testing	4 - 7	Output
C_{zzzz}	Axial stiffness	Biaxial testing	4 - 7	Output
W	Stored strain energy	Biaxial testing	4 - 7	Output
Dist	Distensibility	Biaxial testing	4 - 7	Output

627

628 **Table 2.** Symbols, metrics, methods of acquisition, and sample sizes per condition per time point
 629 ($N =$) for the PLSR model of Lau *et al.*¹⁴ All input and output samples represent mice per time
 630 point and one intestinal segment each. qWB – Quantitative western blotting, IHC –
 631 Immunohistochemistry.

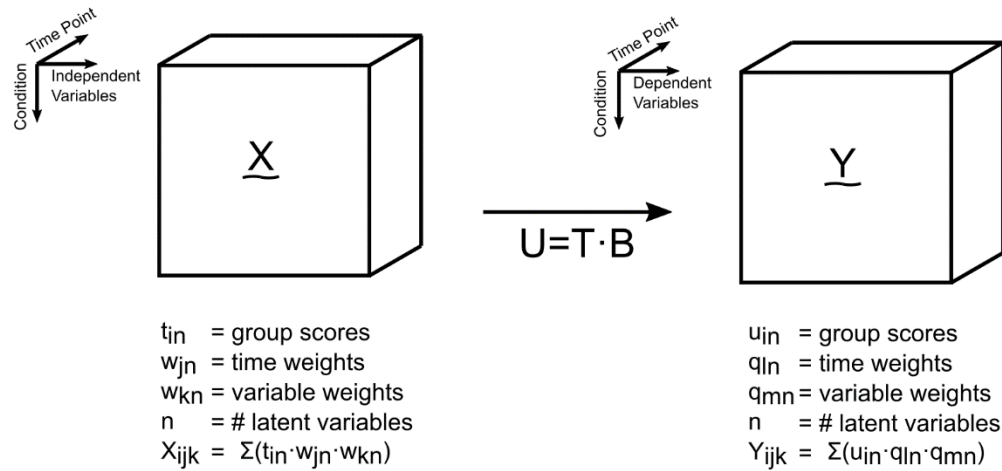
<i>Symbol</i>	<i>Variable Name (Mode 3)</i>	<i>Marker</i>	<i>Method</i>	<i>N =</i>	<i>Input/Output</i>
pI κ B	Inhibitor of nuclear factor κ B- α	Phospho Ser ^{32/36}	Bio-Plex	5	Input
pJnk	c-Jun N-terminal kinase	Phospho Thr ¹⁸³ /Tyr ¹⁸⁵	Bio-Plex	5	Input
pMek1	MAPK and ERK kinase 1	Phospho Ser ^{217/221}	Bio-Plex	5	Input
pErk1/2	Extracellular signal-related kinase 1/2	Phospho Thr ²⁰² /Tyr ²⁰⁴ (1), Thr ¹⁸⁵ /Tyr ¹⁸⁷ (2)	Bio-Plex	5	Input
pRsk	Ribosomal S6 kinase	Phospho Thr ³⁵⁹ /Ser ³⁶³	Bio-Plex	5	Input
pp38	p38 mitogen-activated protein kinase	Phospho Thr ¹⁸⁰ /Tyr ¹⁸²	Bio-Plex	5	Input
pc-Jun	c-Jun	Phospho Ser ⁶³	Bio-Plex	5	Input
pAtf2	Activating transcription factor 2	Phospho Thr ⁷¹	Bio-Plex	5	Input
pAkt	Akt/Protein kinase B	Phospho Ser ⁴⁷³	Bio-Plex	5	Input
pS6	Ribosomal protein S6	Phospho Ser ^{235/236}	Bio-Plex	5	Input
pStat3 ^{S727}	Signal transducer and activator of transcription 3	Phospho Ser ⁷²⁷	Bio-Plex	5	Input
pStat3 ^{Y705}	Signal transducer and activator of transcription 3	Phospho Tyr ⁷⁰⁵	Bio-Plex	5	Input
cc3	Cleaved caspase 3	Cleaved levels	qWB	5	Output
ph3	Phosphorylated histone 3	Number positive cells	IHC	5	Output

632

633 **Table 3.** Symbols, metrics, methods of acquisition, and sample sizes per condition per time point
 634 ($N =$) for the PLSR model of Chitforoushzadeh *et al.*¹³. All input and output data represent cell
 635 extracts per time point. Ab – antibody, μ -array – microarray, qWB – Quantitative western blotting,
 636 CLICK – Cluster Identification via Connectivity Kernels.

Symbol	Variable Name (Mode 3)	Marker	Method	N =	Input/Output
ERK	Extracellular signal-related kinase	Kinase activity	Kinase assay	3 - 6	Input
Akt	Akt/Protein kinase B	Kinase activity	Kinase assay	3 - 6	Input
pAkt _{Ab}	Akt/Protein kinase B	Phospho Ser ⁴⁷³	Ab μ -array	3 - 6	Input
pAkt _{WB}	Akt/Protein kinase B	Phospho Ser ⁴⁷³	qWB	3 - 6	Input
tAkt	Akt/Protein kinase B	Total amount	Ab μ -array	3 - 6	Input
ptAkt	Akt/Protein kinase B	Phospho/total ratio	Ab μ -array	3 - 6	Input
JNK1	Jun N-terminal kinase 1	Kinase activity	Kinase assay	3 - 6	Input
IKK	I κ B kinase	Kinase activity	Kinase assay	3 - 6	Input
MK2	MAP kinase-activated protein kinase 2	Kinase activity	Kinase assay	3 - 6	Input
pMEK	MAPK and ERK kinase 1	Phospho Ser ^{217/221}	qWB	3 - 6	Input
pFKHR	Forkhead in rhabdomyosarcoma	Phospho Ser ²⁵⁶	qWB	3 - 6	Input
PIRS1 ₆₃₆	Insulin receptor substrate 1	Phospho Ser ⁶³⁶	qWB	3 - 6	Input
PIRS1 ₈₉₆	Insulin receptor substrate 1	Phospho Tyr ⁸⁹⁶	qWB	3 - 6	Input
proC8	Caspase-8	Zymogen amount	qWB	3 - 6	Input
cc8	Caspase-8	Cleaved amount	qWB	3 - 6	Input
proC3	Caspase-3	Zymogen amount	qWB	3 - 6	Input
pEGFR	Epidermal growth factor receptor	Phospho Tyr ¹⁰⁶⁸	Ab μ -array	3 - 6	Input
tEGFR	Epidermal growth factor receptor	Total amount	Ab μ -array	3 - 6	Input
ptEGFR	Epidermal growth factor receptor	Phospho/total ratio	Ab μ -array	3 - 6	Input
c1 - c9	Gene clusters 1-9	Transcription level	μ -array + CLICK	2	Output

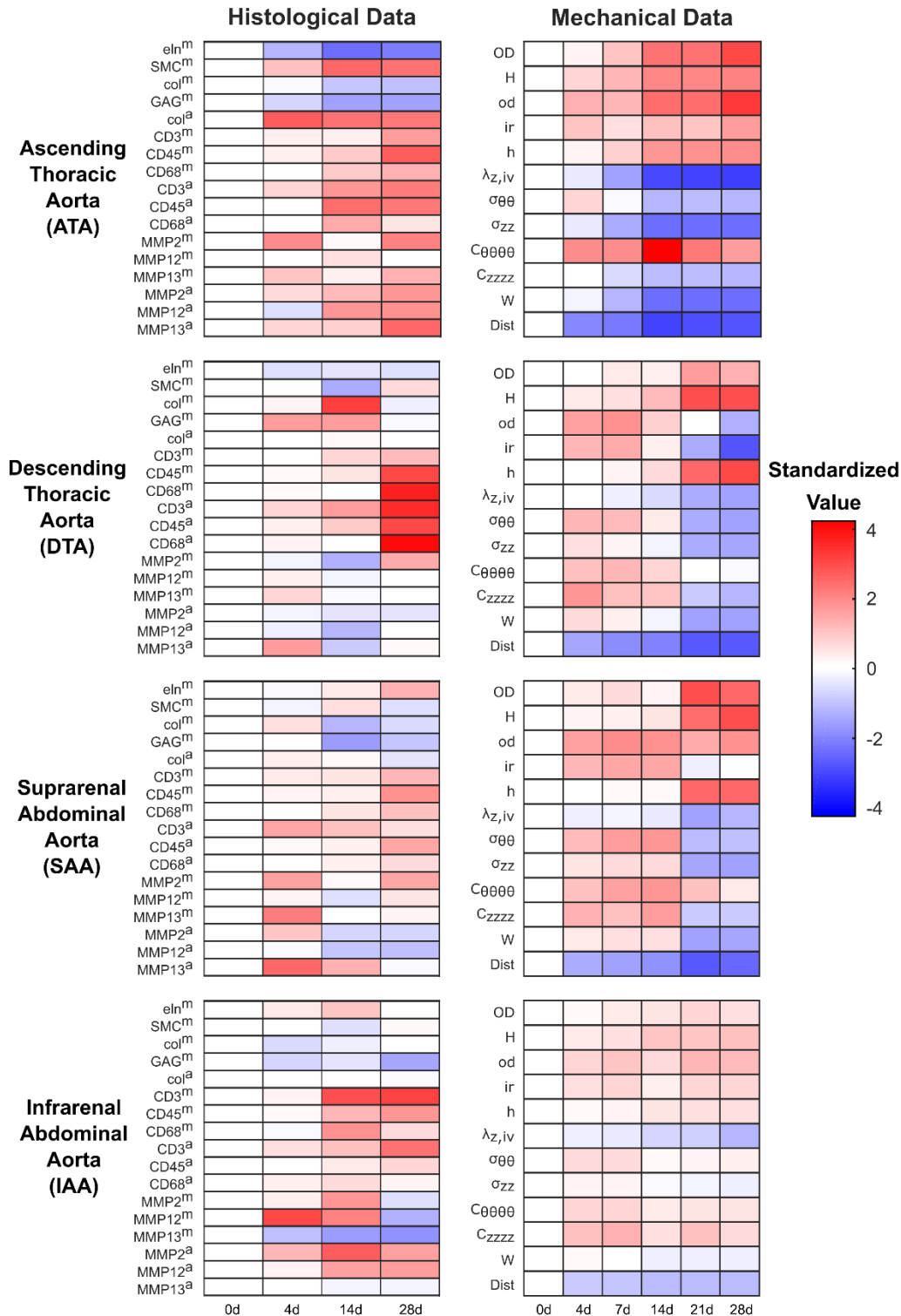
637



638

639 **Figure 1.** A three-mode structure efficiently models dynamic, multivariate data as multi-
 640 dimensional arrays. Data were organized as multidimensional arrays ($\underline{\mathbf{X}}$ and $\underline{\mathbf{Y}}$) with mode 1
 641 (indexed as i) delineating experimental conditions, mode 2 (indexed as j) delineating time course
 642 of experimental endpoints, and mode 3 (indexed as k) delineating variables measured for each
 643 experiment. Independent and dependent variables were selected according to the original datasets
 644 as detailed in Tables 1–3. PLSR derives condition scores (\mathbf{U}) for the dependent data that are
 645 linearly related by regression coefficients (\mathbf{B}) to the scores for the independent data (\mathbf{T}).

646

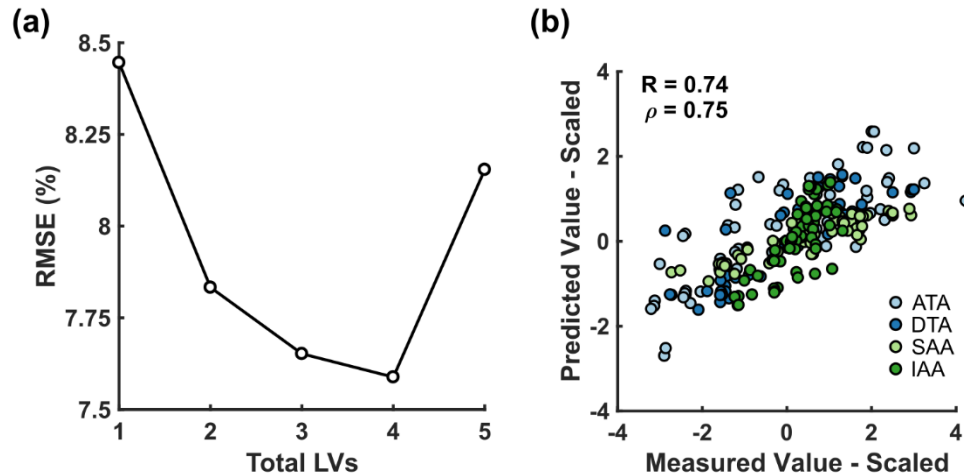


647

648 **Figure 2.** Time-resolved profiling of cellular infiltration, extracellular matrix production–
 649 turnover, and aortic geometry and mechanics during pharmacologically-induced hypertension.
 650 Mice were treated with AngII and tissue harvested at the indicated time points for subsequent

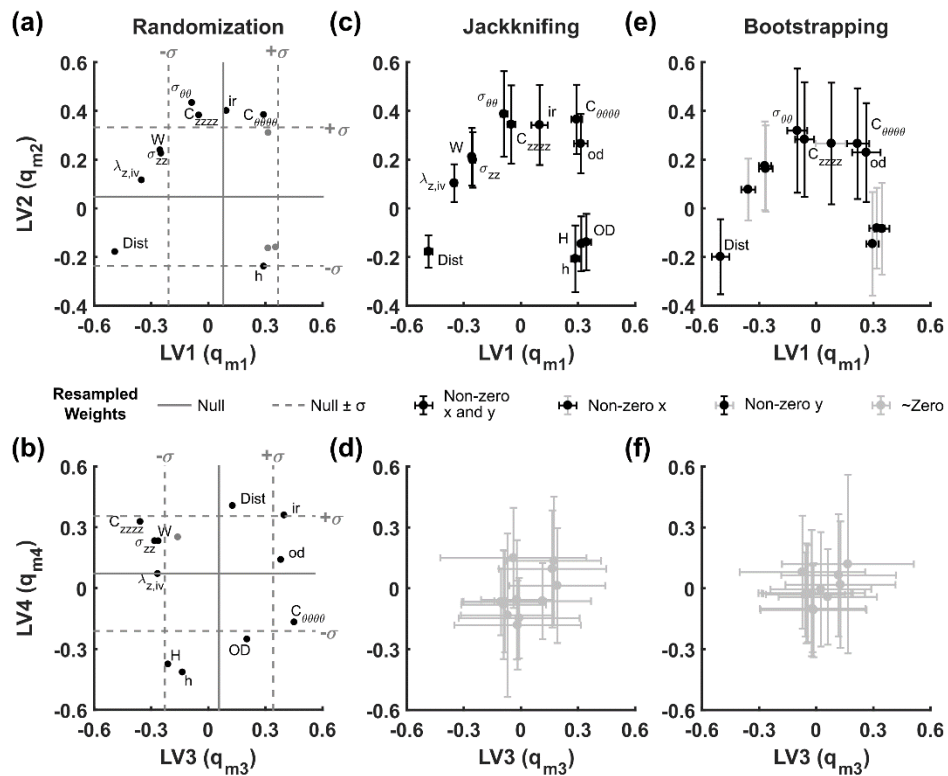
651 histological and mechanical analysis (Table 1). Data are separated by independent (left) and
652 dependent data (right) and aortic region (rows). Standardized differential changes (see Methods)
653 from the 0-day baseline value are shaded red (increase) or blue (decrease).

654



655

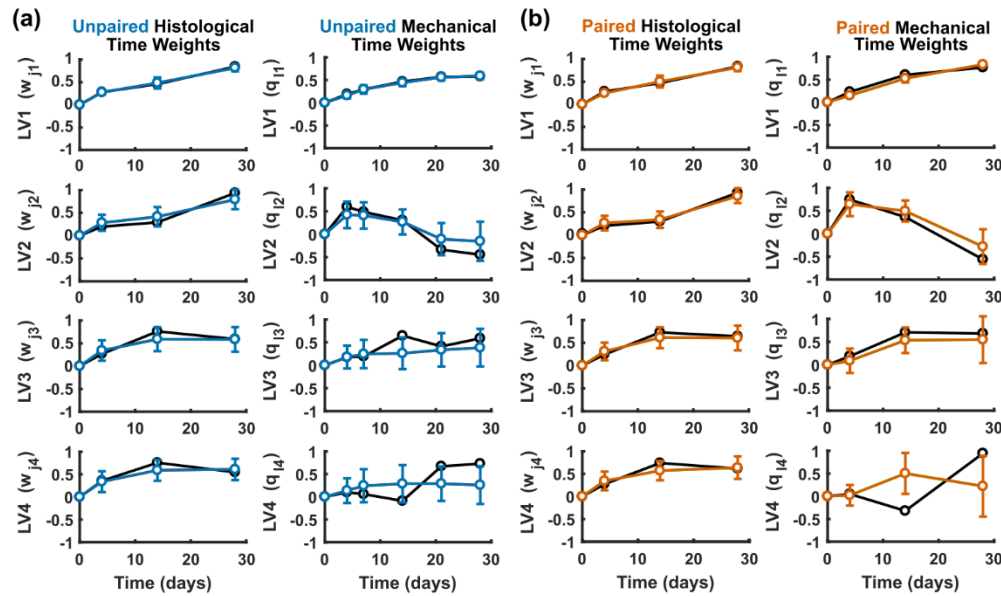
656 **Figure 3.** A four-component multidimensional PLSR model predicts AngII-induced evolution of
657 aortic geometry and mechanics from matrix production and turnover, proteolytic enzyme
658 expression, and inflammatory cell infiltrate. (a) Root mean squared error (RMSE) of cross-
659 validated predictions is minimized with four LVs. (b) Pearson (R) and Spearman (ρ) correlation
660 coefficients of the four-LV PLSR model for all aortic regions and time points. Cross-validated
661 predictions were made by leaving out one entire aortic region at a time. ATA – ascending thoracic
662 aorta, DTA – descending thoracic aorta, SAA – suprarenal abdominal aorta, IAA – infrarenal
663 abdominal aorta.



664

665 **Figure 4.** Resampling PLSR distinguishes robust dependent variable weights (q_{mn}) in a four-LV
 666 model of AngII-induced hypertension. **(a, b)** Generation of a null PLSR model via data
 667 randomization of data to identify parameters of interest. Dependent variable weights (q_{mn}) in the
 668 original PLSR model lying outside of a single standard deviation of the null PLSR model are
 669 labeled in black (see Table 1 for abbreviations). Solid gray lines denote the mean of $N = 500$
 670 reshufflings within mode 1 (*i.e.*, time and measured variables were shuffled within each aortic
 671 region). Dotted-gray lines denote mean \pm standard deviation of weights. **(c, d)** Replicate
 672 resampling ($N = 500$) by jackknifing (“leave one out”) changes confidence of predictions for
 673 parameters compared with randomization. Black dots denote variable weights with error bars that
 674 do not intersect with zero (*i.e.*, parameters weight consistently in a single region). Gray error bars
 675 denote errors that intersect with zero. **(e, f)** Replicate resampling ($N = 500$) by bootstrapping
 676 (“leave one in”) decreases confidence of parameters compared to jackknifing and yields no
 677 significant identifications in LV3 or LV4. Color delineations are identical to those in (c, d). The
 678 top row depicts results for LV1 and LV2, and the bottom row depicts results for LV3 and LV4.

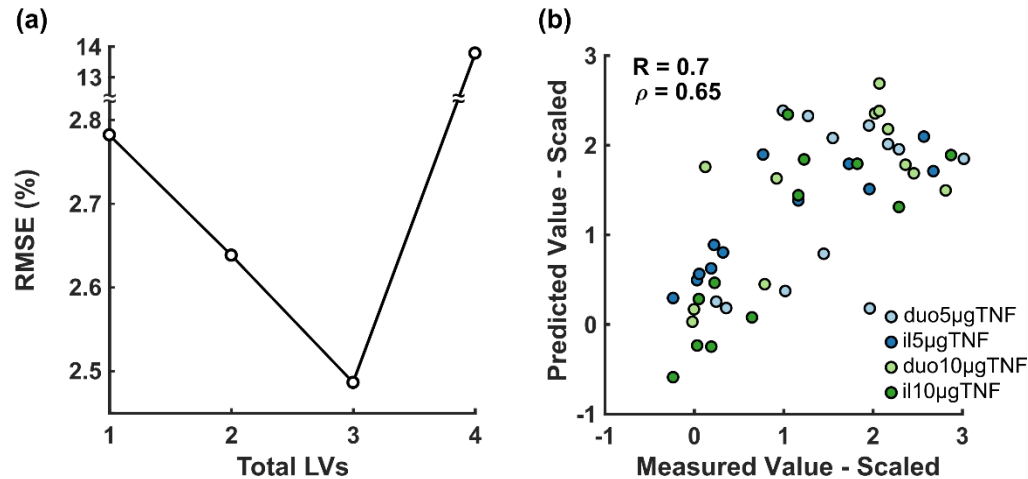
679



680

681 **Figure 5.** Bootstrapping PLSR with paired data shows similar performance to bootstrapping with
 682 unpaired data. Time weights (w_{jn} , q_{ln}) from a PLSR model using (a) unpaired (blue) and (b) paired
 683 (orange) bootstrapping of histological and biomechanical data were generated 500 times for
 684 unpaired and paired sampling each. Note that paired sampling required omission of the 7 and 21
 685 day time points in the dependent variables because histological data were not collected for those
 686 time points. Paired data were available for only two samples per aortic region and time point, both
 687 of which were chosen based on the proximity of the thickness value to the mean thickness value
 688 for the corresponding region and time point.

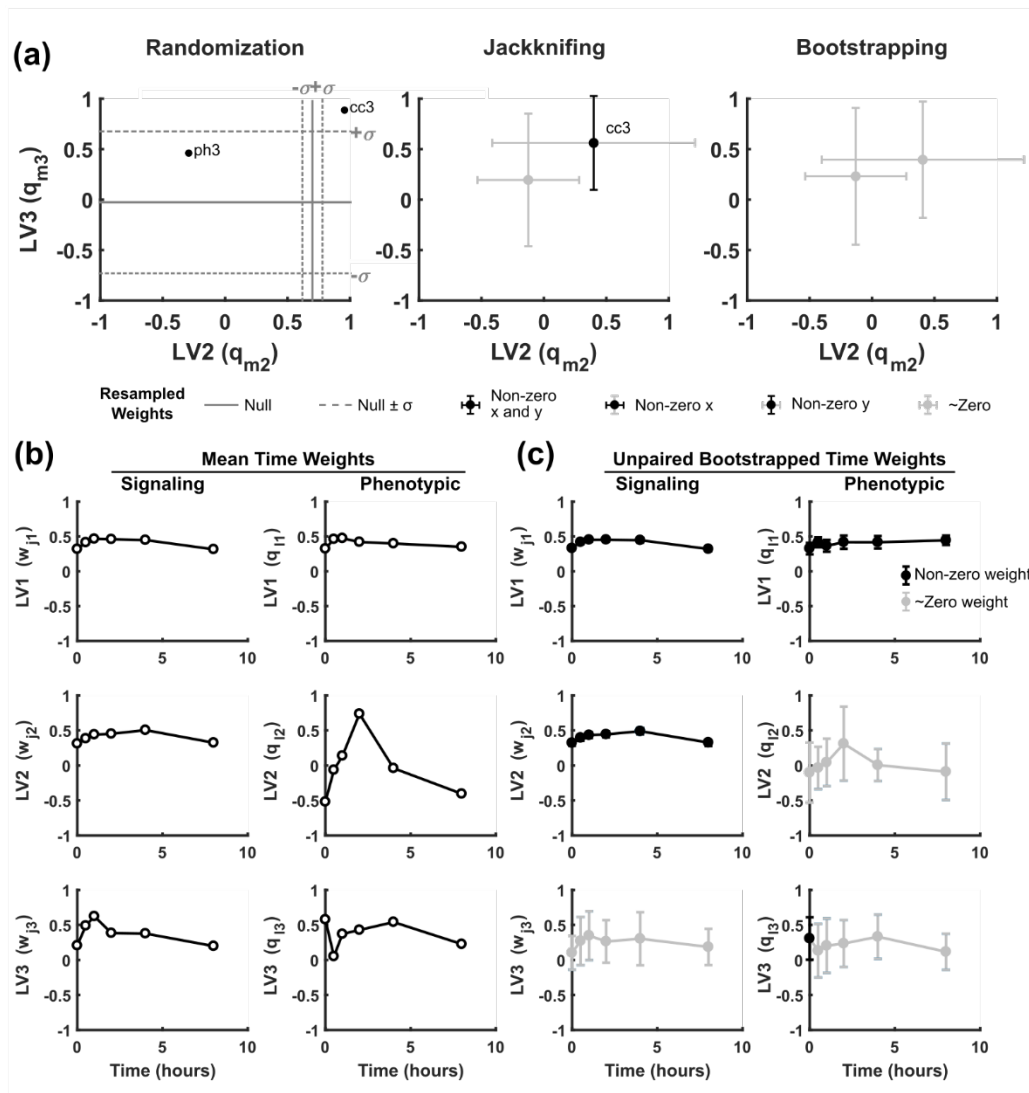
689



690

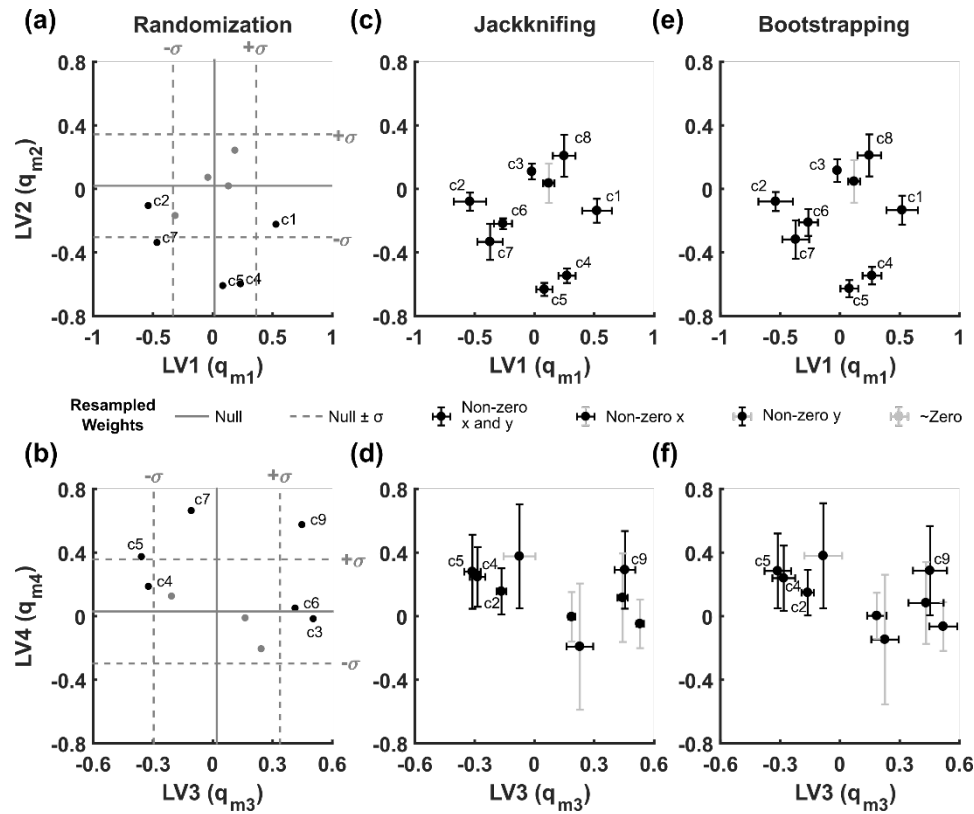
691 **Figure 6.** A three-component multidimensional PLSR model predicts TNF α -induced apoptosis
692 and proliferation of intestinal cells from cell signaling in the duodenum and ileum. **(a)** Root mean
693 squared error (RMSE) of cross-validated predictions is minimized with three LVs. **(b)** Pearson (R)
694 and Spearman (ρ) correlation coefficients of the three-LV PLSR model for all intestinal regions
695 and time points. Cross-validated predictions were made using the leave-one-out approach. duo –
696 duodenum, il – ileum, 5µgTNF – 5 µg TNF α treatment, 10µgTNF – 10 µg TNF α treatment.

697



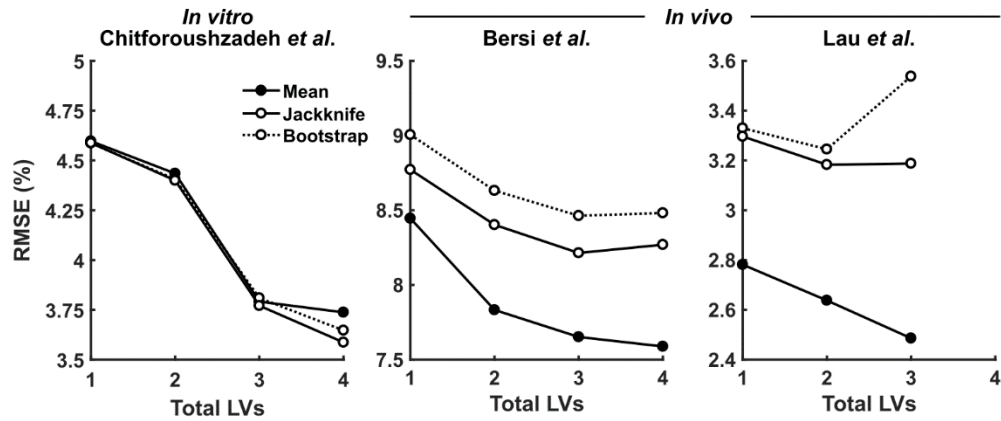
698

699 **Figure 7.** Bootstrapping PLSR of a second *in vivo* dataset reveals poor repeatability in trailing
 700 LVs. **(a)** Dependent variable weights (q_{mn}) for LV2 vs. LV3 following randomization, jackknifing,
 701 and bootstrapping. LV1 is omitted for clarity. Graphs are labeled as in Fig. 4. **(b)** Time weights
 702 for the global-average model delineating temporal behaviors of each LV. **(c)** Bootstrapped time
 703 weights ($N = 500$) show good agreement with the mean dataset on LV1 and LV3 with less
 704 agreement on LV2. Data are presented as mean \pm standard deviation, with black markers indicating
 705 error bars that do not intersect with zero and gray markers indicating error bars that intersect with
 706 zero.



707

708 **Figure 8.** Resampling PLSR validates the robustness of higher-order LVs in multidimensional
 709 arrays. (a, b) Generation of a null PLSR model via randomization ($N = 500$ reshufflings within
 710 mode 1) identifies parameters of interest as variable weights in the original PLSR model (black
 711 dots) lying outside of a single standard deviation of the null PLSR model. (c, d) Replicate
 712 resampling ($N = 500$) by jackknifing (“leave one out”) increases confidence of most LV
 713 parameters. (e, f) Replicate resampling ($N = 500$) by bootstrapping (“leave one in”) yields very
 714 similar results to jackknifing, as expected given the $N = 2$ sample size for output data (Table 3).
 715 Graphs are labeled as in Fig. 4.



716

717 **Figure 9.** Nested resampling PLSR vets the robustness of *in vivo* multidimensional arrays. Root
718 mean squared error (RMSE) as a function of total included LVs is reported for PLSR models of
719 mean datasets (solid lines and filled circles; reprinted from Fig. 3a, 6a, and Chitforoushzadeh *et*
720 *al.*¹³), mean predictions from jackknifed models (solid lines and open circles), and mean
721 predictions from bootstrapped models (dotted lines and open circles).

722